AGU PUBLICATIONS

Geophysical Research Letters

RESEARCH LETTER
10.1002/2017GL075734

Key Points:
- The potential exists to forecast 500 hPa geopotential height at subseasonal to seasonal time scales
- MJO phases 2 and 6 exhibit the most consistent midlatitude response
- The robust teleconnection signals for MJO phases 2 and 6 increase the prediction skill of 500 hPa geopotential height at S2S lead times

Supporting Information:
- Supporting Information S1

Correspondence to:
K.-C. Tseng,
kctseng@rams.colostate.edu

Citation:
Tseng, K.-C., Barnes, E. A., & Maloney, E. D. (2018). Prediction of the midlatitude response to strong Madden-Julian oscillation events on S2S time scales. *Geophysical Research Letters*, *45*, 463–470. https://doi.org/10.1002/2017GL075734

Received 18 SEP 2017
Accepted 20 DEC 2017
Accepted article online 27 DEC 2017
Published online 15 JAN 2018

Prediction of the Midlatitude Response to Strong Madden-Julian Oscillation Events on S2S Time Scales

K.-C. Tseng[1], E. A. Barnes[1], and E. D. Maloney[1]

[1]Department of Atmospheric Science, Colorado State University, Fort Collins, CO, USA

Abstract The Madden-Julian Oscillation (MJO) forces strong variations in extratropical atmospheric circulations that have important implications for subseasonal-to-seasonal (S2S) prediction. In particular, certain MJO phases are characterized by a consistent modulation of geopotential height in the North Pacific and adjacent regions across different MJO events. Until recently, only limited research has examined the relationship between these robust MJO tropical-extratropical teleconnections and model prediction skill. In this study, reanalysis data and numerical forecast model ensemble hindcasts are used to demonstrate that robust teleconnections in specific MJO phases and time lags are also characterized by excellent agreement in the prediction of geopotential height anomalies across model ensemble members at forecast leads of up to 3 weeks. These periods of enhanced prediction capabilities extend the possibility for skillful extratropical weather prediction beyond traditional 10–13 day limits.

1. Introduction

The traditional view of midlatitude numerical weather prediction maintains that the nonlinear growth of errors from uncertainty in initial conditions, or deficiency of physical processes in numerical models, makes weather unpredictable beyond a 10–13 day lead time (e.g., Hamill & Kiladis, 2014). Nevertheless, an increasing number of studies have demonstrated that information from lower-frequency variability (lower frequency referring to a period longer than about 7 days), such as the seasonal cycle, land processes, or air-sea interactions can extend model prediction skill beyond this traditional predictability limit (Chen & Dudhia, 2001; Infanti & Kirtman, 2016; Jin et al., 2014). Among these low-frequency time scales, subseasonal-to-seasonal (S2S hereafter) time scales are of particular interest not only because we have less confidence in prediction at these time scales (Vitart, 2014) but also because they serve as a bridge between weather and climate.

The Madden-Julian oscillation (MJO) is an equatorial propagating convective envelope characterized by periods of 30–90 days (Adames & Kim, 2016; Hendon & Salby, 1994), a band that fortuitously occurs in the S2S window with lower traditional prediction skill. A particular motivation for improving S2S prediction is that some of the most persistent and impactful weather phenomena in midlatitudes (e.g., blocking anticyclones, Berggren et al., 1949; Masato et al., 2012, or extratropical storms) are associated with low-frequency variations of geopotential height, which can be driven by tropical-extratropical teleconnections. MJO-related teleconnections have significant impacts on S2S time scale geopotential height anomalies in the midlatitude Pacific and North America, which consequently modulate the weather patterns of those regions (Henderson et al., 2017; Seo & Lee, 2017). For example, previous research has shown that when the MJO exhibits enhanced convection in the western Pacific and suppressed convection in the eastern Indian Ocean, positive geopotential height anomalies generated by stationary Rossby waves occur in the Gulf of Alaska, which can dramatically increase the occurrence of blocking (Henderson et al., 2016). Further, some studies have shown that improved MJO forecasts have positive impacts on midlatitude weather forecasts (Hendon et al., 2000; Vitart & Molteni, 2010).

Understanding the teleconnected response of the MJO does present challenges, however. The MJO is a circumnavigating system and the teleconnection signal takes time to propagate to the midlatitudes. Hence, a location in the midlatitudes may exhibit a teleconnected response that was initiated by tropical convective heating in an earlier phase of the MJO. The highly varied features of the MJO combined with its teleconnections make it difficult to quantify the MJO's influence over different phases and lead times, an issue especially

important for midlatitude prediction. Thus, although there have been numerous studies showing how MJO-related teleconnections modulate midlatitude regions (Henderson et al., 2017; Kim et al., 2006; Seo & Lee, 2017), studies illustrating the MJO teleconnection influence on the forecast skill of numerical weather prediction models in the North Pacific and adjacent regions are still limited.

Here we demonstrate that while some MJO phases produce robust teleconnections in the midlatitudes, others do not. By robust, we mean generating consistent patterns over different events. This result is shown in reanalysis data, and its implications for S2S forecasting are demonstrated using a hindcast ensemble from the European Centre for Medium-Range Weather Forecasts (ECMWF) forecast model. Specifically, MJO phases in which tropical-extratropical teleconnections are more robust at lead times of 2–3 weeks in the reanalysis are also the phases that offer improved prediction of the North Pacific midlatitude circulations in the ECMWF ensemble forecast system.

2. Data and Methods

2.1. Data

This study uses daily 500 hPa geopotential height (Z500) from Modern-Era Retrospective Analysis for Research and Applications (MERRA hereafter) (Rienecker et al., 2011) and ECMWF ensemble hindcasts (Vitart et al., 2017). The ensemble hindcasts were acquired from ECMWF's S2S data library established by the World Weather Research Program/World Climate Research Program (WWRP/WCRP), which includes 11 different hindcast models. The ECMWF ensemble hindcast system is the most ideal model for our research because it has the second most ensemble members and reforecasts frequently enough for MJO events sampling (4 times/week). All of the data sets mentioned above were interpolated to daily time scales and 2.5^o by 2.5^o horizontal resolution.

Since the MJO teleconnection signals are stronger in boreal winter over the North Pacific, we only use the data in the extended boreal winter (November–March) from 1979 to 2015 for MERRA. To remove the influence of the annual cycle, we first calculate the daily climatology of Z500 and define the annual cycle as the first three harmonics of this time series. Anomalies are computed by subtracting the annual cycles from the raw Z500. For the ECMWF ensemble hindcast (10 perturbed ensemble members), the Z500 is preprocessed in the same way as reanalysis data, where the daily climatology is derived from the ensemble mean as a function of lag. The hindcast data cover the period from 1999 to 2015. In this study, the MJO phase is defined by the OLR MJO index (OMI) (Kiladis et al., 2006) and only days with an amplitude of OMI greater than 1 standard deviation are included in the composites.

2.2. Methods

The composited anomalous Z500 is derived by averaging anomalies for days with OMI amplitude greater than 1 standard deviation at lag zero over different MJO phases and time lags. In the reanalysis, the sample sizes for the eight MJO phases (in order from 1 to 8) are 388, 415, 426, 435, 352, 430, 441, and 429 (and 2,265 days for non-MJO events). If the amplitudes of the OMI are consecutively greater than 1 standard deviation, they are considered as one event (each phase is accounted for separately). The total number of events for each MJO phase (in order from 1 to 8) are 100, 107, 103, 102, 106, 108, 103, and 106, respectively. To assess statistical significance, a bootstrapping analysis is employed. We randomly choose days in the extended boreal winter (November–March) from 1979 to 2015 based on the number of MJO events in each of the eight phases. By averaging the Z500 for randomly selected days based on these numbers, and repeating this process 500 times, we can approximate the distribution of the sample mean. Then, the 95% confidence bounds on the geopotential height anomalies are determined from this distribution (Wilks, 2011).

We quantify the pattern robustness over different events by calculating the area-weighted anomaly correlations between two maps. The pattern robustness is then defined as the fraction of pairs with correlation greater than 0.5, although conclusions are not sensitive to this threshold. For the pattern correlations, a similar significance test is employed to approximate the distribution of the percentage of pairs with high correlation coefficients. Details of the preprocessing of the data for Figure 3 is given in the main text.

3. Results

3.1. Pattern Consistency of the Teleconnected Z500 in MERRA Reanalysis

Figure 1 shows a composite map of Z500 for the extended boreal winter. Each panel denotes a different MJO phase and/or time lag where an *n* day lag represents *n* days after the given MJO phase. Dotted regions

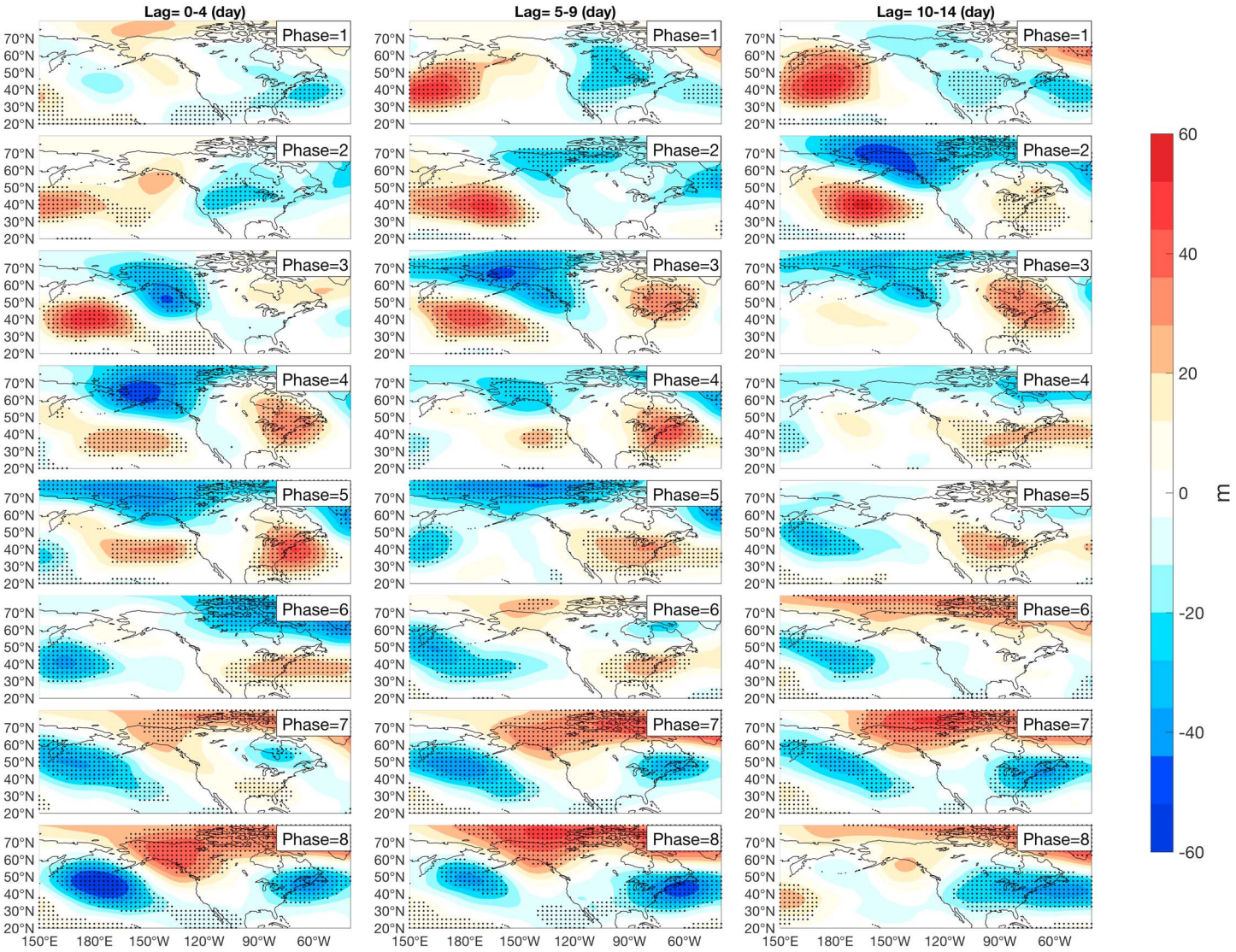

Figure 1. MJO phase composite of anomalous 500 hPa geopotential height for lag 0–4 days after an MJO event, lag 5–9 days, and lag 10–14 days. The dotted regions denote the anomalies that are significantly different from zero at 95% confidence based on bootstrapping analysis.

indicate anomalies that are significantly different from zero at the 95% level based on a bootstrapping analysis (see section 2). In Figure 1, the spatial pattern of Z500 with significant tropical-extratropical teleconnection signals (dotted regions), such as phase 2, lag 10–14 or phase 3, lag 5–9, shows a wave train structure with three centers located in the North Pacific, the Gulf of Alaska, and the eastern U.S., which have been documented in many previous numerical and observational studies (e.g., Henderson et al., 2016; Hoskins & Karoly, 1981; Kim et al., 2006; Wallace & Gutzler, 1981). These signals initiate from the midlatitude Pacific in a region of high-pressure anomalies (e.g., phase 2, lag 5–9) and then low-pressure anomalies in the Gulf of Alaska and the U.S. West Coast subsequently strengthen (e.g., phase 2, lag 10-14), which highlights the vital role of MJO anomalous heating in connecting low-latitude and midlatitude regions. Since the MJO is a circumnavigating system on the equator, where one phase is often followed by the next phase and each phase typically lasts for 3–5 days, some similarity of composite patterns occurs along diagonals in Figure 1 from the upper right to the lower left (e.g., phase 2, lag 10–14 is similar to phase 3, lag 5–9). A nearly identical, but opposite, teleconnection pattern can be observed in phases 7 and 8 compared with phases 2 and 3, caused by opposite-signed MJO anomalous heating in the tropics.

Figure 1 shows that the composited amplitude of Z500 exhibits larger areas of significance over specific MJO phases and lags. There are a couple reasons why this could be the case: (1) the strong Z500 variations are

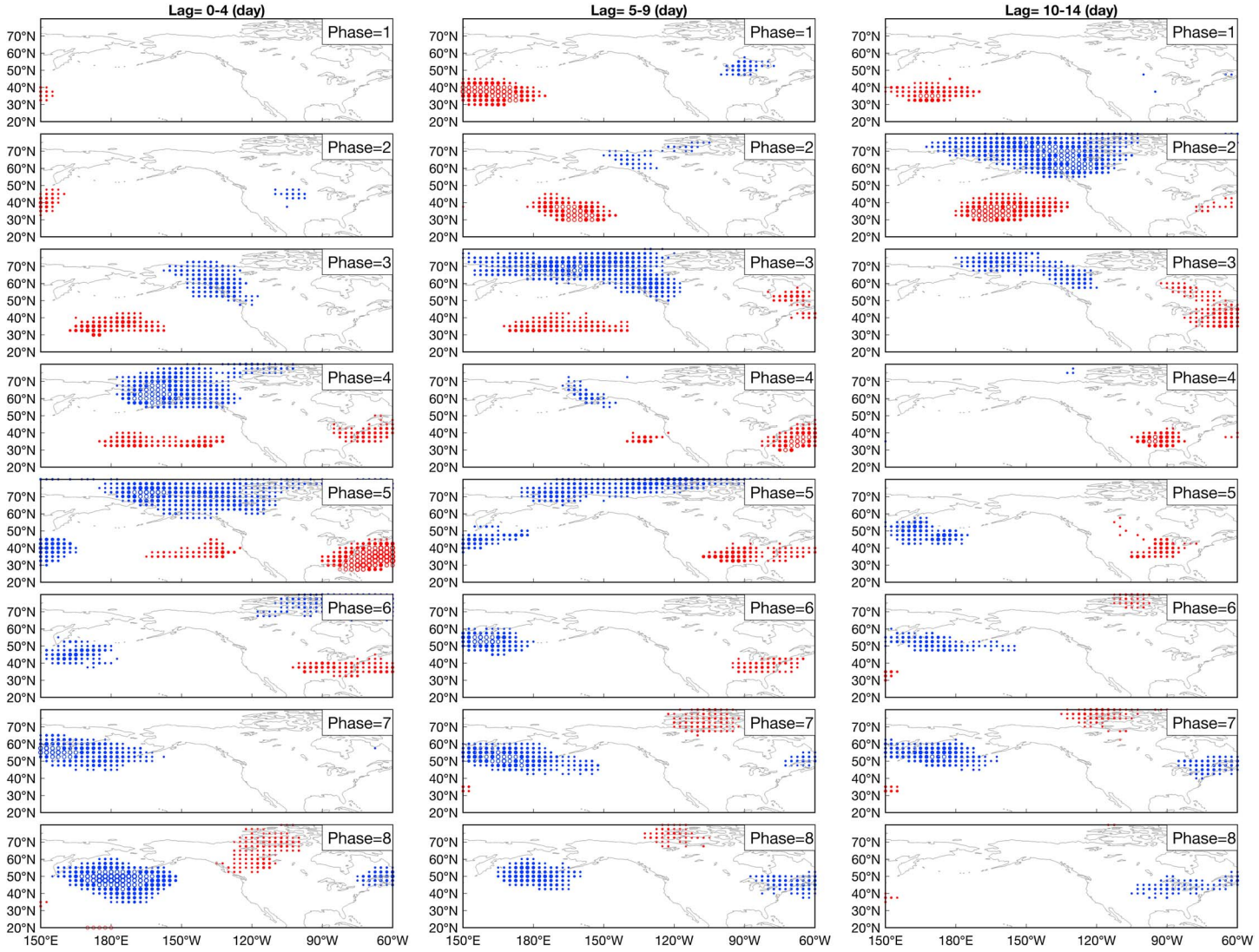

Figure 2. The sign agreement of anomalous Z500 over different MJO events and lags. Red (blue) dots indicate positive (negative) geopotential height anomalies with occurrence frequency >65%. Open circles indicate an occurrence frequency >75%.

dominated by only a few MJO events, or (2) certain phases of the MJO produce more consistent Z500 patterns compared to other MJO phases. The latter is more beneficial than the former for weather prediction, because it implies that particular MJO phases may be more robust, and thus support extended range predictability. To test whether the occurrence frequency of positive and negative geopotential height anomalies in the North Pacific change with MJO phase, we estimate the corresponding frequencies at each grid point over different phases and lags using daily data. Figure 2 shows grid points where positive or negative anomalies occur over at least 65% of all events. In Figure 2, the dotted regions present a wave train pattern extending from the North Pacific to the Gulf of Alaska which is consistent with Figure 1 (e.g., phase 2, lag 10–14 and phase 3, lag 5–9). Some regions in the wave train pattern exceed 75% frequency (hollow dots) such as the centers of high-pressure anomaly in the North Pacific and low-pressure anomaly in the Gulf of Alaska at phase 2, lag 10–14. On the other hand, the regions with low-occurrence frequency (without dots) are also the regions with insignificant composited anomalies in Figure 1. In addition, at lag 10–14, which is the traditional limit of weather predictions, some phases (e.g., phases 2 and 7) demonstrate high preference of a Rossby wave train pattern, while others do not (e.g., phases 4 and 8). These results suggest that extended predictions may be possible for certain MJO phases.

Nevertheless, the result in Figure 2 is not enough to show the pattern consistency over different MJO events, since the sign consistency is calculated on a local basis with no knowledge of the large-scale pattern.

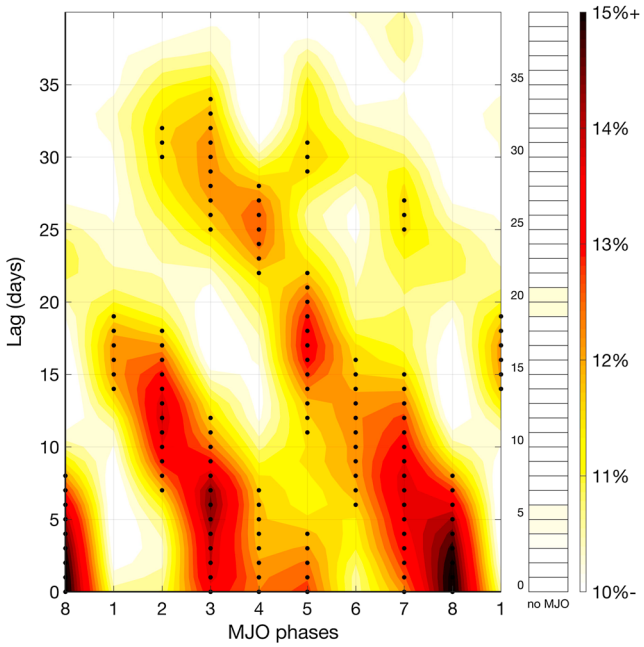

Figure 3. The pattern agreement of Z500 over different MJO events quantified using pattern correlations. Shading indicates the occurrence frequency of any two events exhibiting a correlation coefficient >0.5. Dotted regions indicate an occurrence frequency that is significantly higher than climatology at the 99% significance level based on a bootstrapping analysis.

To quantify the robustness of the teleconnected patterns, we calculate paired pattern correlations in the North Pacific (150°E–120°W, 20°N–70°N) over different phases and time lags. For each phase and lag, one pattern correlation coefficient is derived from every two events. Thus, if there are m events, the number of combinations will be $C_2^m = \frac{m\cdot(m-1)}{2}$. By calculating the number of paired combinations that exceed a correlation of 0.5, we quantify the consistency of the Z500 patten across MJO phases. Figure 3 shows the result of the paired correlation analysis. Dark (light) colors indicate more (fewer) pairs with high pattern correlations and dotted regions denote where the number of high correlations exceed the 99% confidence bounds by bootstrapping analysis. The shaded regions show stair-like patterns with a slope of 5 days per phase, which is the typical phase duration of the MJO. Using phase 2 as an example, the transition from light colors (lag 1–7) to dark colors (lag 8–15) indicates an increasing influence of robust tropical-extratropical teleconnections in modulating the midlatitude Z500 pattern as well as the increased pattern consistency 8–15 days following MJO phase 2. A remarkable fact of Figure 3 is that it provides more information than previous studies which showed that the Pacific North American (PNA) pattern is more likely to occur after MJO phase 2 and phase 6 by composite analysis. First, the daily Z500 is a highly varying field. Thus, even though composite maps may show a PNA-like pattern, it is unclear how much any one event will actually look like the PNA pattern. However, Figure 3 shows phase-dependent pattern consistency without supposing a PNA or any other pattern. Second, the phase-dependent pattern consistency gives us a new perspective on the extended range prediction since it indicates that the Z500 pattern over specific phases (e.g., phases 2 and 6) might be more predicable than others (e.g., phases 4 and 8).

3.2. Ensemble Agreement of Z500 in ECMWF Ensemble Hindcast

Our analysis of the MERRA reanalysis demonstrates that tropical-extratropical teleconnection patterns driven by the MJO are more robust for specific MJO phases and time lags compared to others. With this observational result in mind, we next address whether the prediction skill of Z500 in the North Pacific in a numerical weather prediction model is improved for MJO phases with more robust teleconnections. Therefore, we examine how the MJO's tropical-extratropical teleconnections influence Z500 prediction skill as a function of MJO phase in the ECMWF model ensemble hindcasts. We note that the prediction skill is not only a function of the teleconnection robustness but also a function of error growth due to inaccuracies in the initial conditions, model physics and truncation errors.

In order to quantify the robustness of the model's composite MJO teleconnections, we divide the ECMWF ensemble hindcasts (1999–2015) into 10 groups, arbitrarily selected on the basis of ensemble member number. Then, we compute the average composite pattern and agreement in sign across the 10 groups (Figure 4). Here an n day lead represents not only n days after a given MJO phase but also n days after the simulation was initialized. Red-dotted (blue-dotted) regions indicate where all of the ensemble members agree on the sign (i.e., positive or negative) of the composited Z500 anomalies. We note that most of the regions with high ensemble agreement also agree with the sign of anomalous Z500 in the reanalysis (not shown). The dot size shows the amplitude of the ensemble-mean Z500. In Figure 4, the dots are generally evenly distributed in the domain immediately after the initialization time (lead 0–4) for both MJO phases 2 and 4, which indicates that all 10 ensemble members agree on the composite pattern. As the lead time increases, phase 2 continues to show widespread areas of high agreement including the high-pressure anomaly in the North Pacific. In particular, these regions show a wave train pattern that is very similar to the composited Z500 pattern in Figure 1 (phase 2 and lag 10–14). This high agreement on the wave train pattern even exists at lead times 15–19 of phase 2. In contrast to phase 2, the dots for phase 4 become more sparse with increasing lead time and there are few grid points with large Z500 amplitude. This tendency becomes clearer for lead times 10–14 and 15–19 when little ensemble agreement exists for phase 4. Hence, Figure 4 provides evidence that the current ECMWF forecast system has strong ensemble member agreement for the composited teleconnected geopotential height anomalies at leads of greater than 2 weeks for certain phases of the MJO.

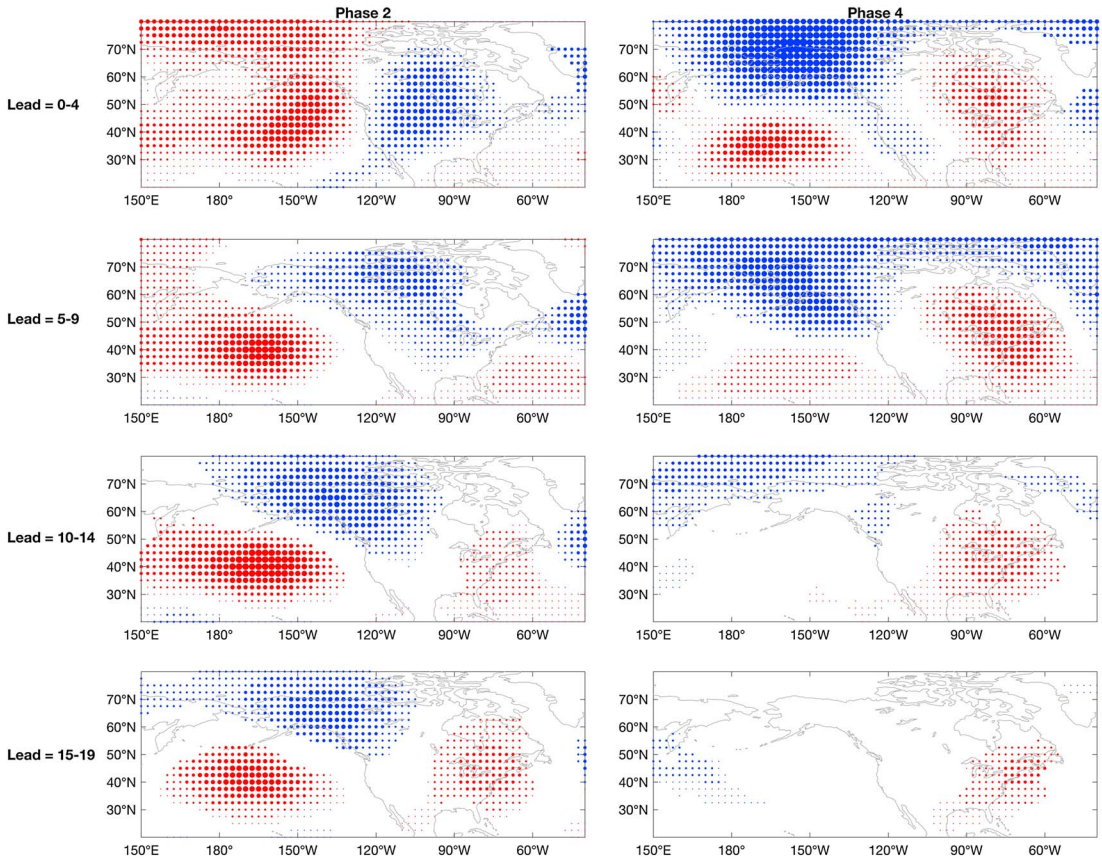

Figure 4. Composites of Z500 over ECMWF's 10 ensemble members for MJO phases 2 and 4. Dotted regions indicate all (10) ensemble members, and the MERRA reanalysis agree on the sign of the anomaly and the dot size is defined by the ensemble-averaged amplitude of composite Z500. Small: amplitude < 40 m, Median: 40–70 m, and Large: >70 m. Blue shading denotes negative anomalies, while red shading denotes positive anomalies.

Figure 4 is based on the composite pattern of Z500, which only provides a general picture of how MJO-related teleconnections may influence the prediction skill of the mean pattern. However, Z500 variations on a daily basis may not necessarily be modulated as consistently as in the composite sense. Therefore, we reexamine the concepts in Figures 3 and 4 for individual MJO events instead of the composite fields. First, we calculate pattern correlation coefficients between the daily ensemble mean and the daily observed Z500 from MERRA for every event. We then calculate and plot the percent of the correlations that are greater than zero as a function of model lead time and MJO phase (a sensitivity test of different correlation thresholds was also tested and the results are presented in the supporting information and Figure S1). The result is shown in Figure 5, where dark colors indicate higher frequencies of positive correlations between the model forecast and what was observed, and dots indicate regions that are 99% significantly higher than the randomly sampled data by bootstrapping. To assess significance, we apply bootstrapping analysis under the null hypothesis that the chance of predicting positive correlation coefficients is the same over different events at the same model lead time. Days including the events with and without strong MJOs are randomly sampled according to the numbers of MJO events at different phases and lead times. By resampling data 500 times, we can approximate the distribution of correlations under the null hypothesis.

Two distinct features are evident in Figure 5. First, the color of shading goes from dark red to light yellow, which is associated with the decrease of prediction skill with time. This is also seen in Figure 4, which shows fewer dots with increasing model lead time. In addition to the decrease of prediction skill, the second prominent feature is that extended skill is found in selected MJO phases; for example, phases 1 and 2 show longer lead time with higher prediction skill than phases 4 and 8. Several possible explanations exist for this phase-dependent prediction skill. One explanation is associated with model error growth. Robust teleconnections might not only modulate the Z500 patterns over different events but also reduce the ensemble spread. (An equivalent of Figure 3 for the ECMWF reforecast was made and the results are presented in the supporting information;

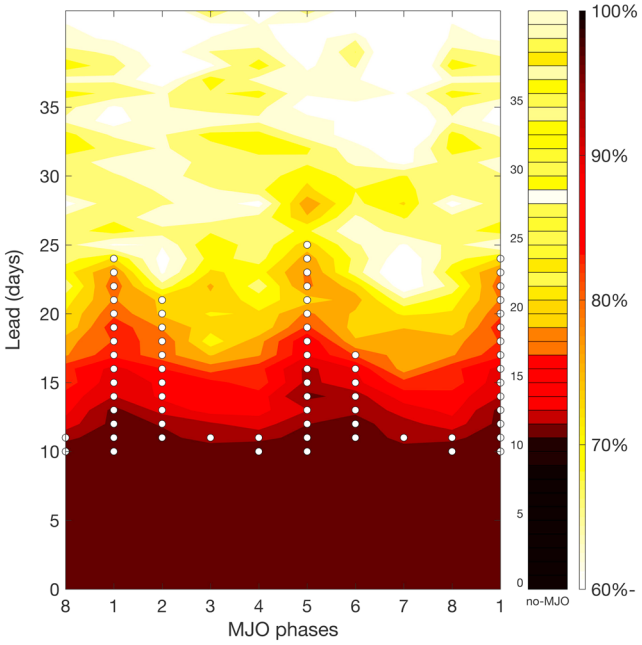

Figure 5. The frequency (as a percentage) with which the Z500 pattern predicted by the ECMWF ensemble mean is positively correlated with the observed Z500 anomalies from MERRA reanalysis. The dotted regions indicates that the value is significantly higher at 99% confidence than the randomly sampled data at the same lead time by bootstrapping analysis. The sample sizes for each MJO phase are (in order from 1 to 8) 89, 110, 112, 115, 86, 98, 108, and 110.

Figure S2.) With such robust teleconnections, the ratio of the teleconnection signal to the noise introduced by the initial perturbations stays large enough to produce skillful forecasts up to 3 weeks later. This point is also supported by Figure 4: all ensemble members hindcast a robust wave train pattern at phase 2 and lead times 15–19. For phases without robust teleconnections, such as phase 4 (Figure 3), the ensemble spread grows much faster than the phases with robust teleconnections. However, one might wonder why phase 4 has high pattern consistency at lead times 22–30 (Figure 3) but relatively low prediction skill (Figure 5). One possible reason for this behavior is that the phase 4 teleconnection only becomes robust at 22–30 days after an event (Figure 3). Thus, the model error might be too large at 22–30 days after the initialization to take advantage of the information from a robust teleconnection. The second explanation is related to the traditional "Maritime Continent prediction barrier." Previous studies have shown that most numerical models have difficulty in simulating MJO propagation across the Maritime Continent due to coarse model resolution and poorly simulated scale interactions (Kim et al., 2016; Peatman et al., 2015), which might cause unrealistic large-scale circulation anomalies in the upper troposphere and negatively impact the Rossby wave source that produces tropical-extratropical teleconnections. A third possible explanation is associated with the sensitivity of the teleconnection produced by anomalous tropical heating to the mean state. Research has shown that the relative position of anomalous heating and the subtropical jet is a key factor in determining the nature of tropical- extratropical teleconnections (Henderson et al., 2017). In general, all of these factors can limit the prediction skill of numerical models: the former implies that a large signal (teleconnection) to noise (error growth) ratio is required to have skillful extended predictions; the latter two factors imply that if the model cannot simulate the MJO or mean state with fidelity, it will not produce reasonable teleconnection signals that provide skillful extended predictions.

4. Discussion and Conclusions

The results shown here indicate that MJO convection can produce a robust modulation of Z500 in the North Pacific for certain phases and time lags. This phase-dependent modulation of Z500 by the MJO is also reflected in an MJO phase and forecast lead dependence in ECMWF forecast model's ensemble agreement and prediction skill. A robust tropical-extratropical teleconnection at MJO phases 1, 2, 5, and 6 provides more confidence in the prediction of Z500 at 2 to 3 week leads, which is longer than that associated with the traditional 10–13 day midlatitude "predictability barrier." However, the prediction skill is not increased at all phases and lead times at which reanalysis fields indicated high pattern consistency (e.g., phases 4). The factors responsible for diminished prediction skill at MJO phase 4 relative to that suggested by reanalysis fields remain to be determined. Nevertheless, our results show that MJO-related tropical-extratropical teleconnections clearly have profound implications for understanding and predicting S2S time scale variability over the North Pacific and North America.

The insight we have gained about the phase-dependent MJO modulation of Z500 has important implications and also suggests some interesting questions for future work. For the high-frequency weather phenomena influenced by the midlatitude geopotential height variations, such as atmospheric rivers (Mundhenk et al., 2016) and blocking anticyclones (Henderson et al., 2016), we may expect some similarities between their prediction skill and that of Z500. This is an area of ongoing research. Low-frequency variability (longer than intraseasonal time scales) associated with phenomena such as the quasi-biennial oscillation (QBO) or El Niño–Southern Oscillation (ENSO) are also likely to modulate the nature of MJO teleconnections (Baggett et al., 2017; Moon et al., 2011; Son et al., 2017). Furthermore, the interaction between MJO heating and the position of east Asia jet presents a challenge for midlatitude teleconnection predictions, given changes in jet position and strength from year to year. Although subject to the uncertainties of scale interactions and nonlinear error growth in numerical models, the robust impacts of the MJO on midlatitude geopotential height, and thus the midlatitude circulation and steering flow, provides the scientific community useful tools for subseasonal-to-seasonal prediction.

Acknowledgments
This research has been conducted as part of the NOAA MAPP S2S Prediction Task Force and supported by NOAA grant NA16OAR4310064. This research is also supported by NSF's Climate and Large-scale Dynamics Program grant AGS-1441916. We thank Cory Baggett, Bryan Mundhenk, and Kyle Nardi for their great help in acquiring the data and NASA's Global Modeling and Assimilation Office and Goddard Earth Sciences Data and Information Services Center (http://disc.sci.gsfc.nasa.gov/) for the MERRA reanalysis data. We also thank S2S Project established by the World Weather Research Program/World Climate Research Program (WWRP/WCRP) for organizing the ECMWF reforecast. The ECWMF reforecast and S2S Project can be found online at https://software.ecmwf.int/wiki/display/S2S/Models.

References

Adames, Á. F., & Kim, D. (2016). The MJO as a dispersive, convectively coupled moisture wave: Theory and observations. *Journal of Atmospheric Sciences*, *73*, 913–941.

Baggett, C. F., Barnes, E. A., Maloney, E. D., & Mundhenk, B. D. (2017). Advancing atmospheric river forecasts into subseasonal-to-seasonal time scales. *Geophysical Research Letters*, *44*, 7528–7536. https://doi.org/10.1002/2017GL074434

Berggren, R., Bolin, B., & Rossby, C.-G. (1949). An aerological study of zonal motion, its perturbations and break-down. *Tellus*, *1*, 14–37.

Chen, F., & Dudhia, J. (2001). Coupling an advanced land surface–hydrology model with the Penn State–NCAR MM5 modeling system. Part I: Model implementation and sensitivity. *Monthly Weather Review*, *129*, 569–585.

Hamill, T. M., & Kiladis, G. N. (2014). Skill of the MJO and Northern Hemisphere blocking in GEFS medium-range reforecasts. *Monthly Weather Review*, *142*, 868–885.

Henderson, S. A., Maloney, E. D., & Barnes, E. A. (2016). The influence of the Madden–Julian oscillation on Northern Hemisphere winter blocking. *Journal of Climate*, *29*, 4597–4616.

Henderson, S. A., Maloney, E. D., & Son, S.-W. (2017). Madden-Julian oscillation Pacific teleconnections: The impact of the basic state and MJO representation in general circulation models. *Journal of Climate*, *30*(12), 4567–4587.

Hendon, H. H., & Salby, M. L. (1994). The life cycle of the Madden-Julian Oscillation. *Journal of Atmospheric Sciences*, *51*, 2225–2237.

Hendon, H. H., Liebmann, B., Newman, M., Glick, J. D., & Schemm, J. (2000). Medium-range forecast errors associated with active episodes of the Madden–Julian oscillation. *Monthly Weather Review*, *128*, 69–86.

Hoskins, B. J., & Karoly, D. J. (1981). The steady linear response of a spherical atmosphere to thermal and orographic forcing. *Journal of Atmospheric Sciences.*, *38*, 1179–1196.

Infanti, J. M., & Kirtman, B. P. (2016). North American rainfall and temperature prediction response to the diversity of ENSO. *Climate Dynamics*, *46*, 3007–3023.

Jin, F.-F., Boucharel, J., & Lin, I.-I. (2014). Eastern Pacific tropical cyclones intensified by El Niño delivery of subsurface ocean heat. *Nature*, *516*, 82–85.

Kiladis, G. N., Dias, J., Straub, K. H., Wheeler, M. C., Tulich, S. N., Kikuchi, K., … Ventrice, M. J. (2006). A comparison of OLR and circulation based indices for tracking the MJO. *Monthly Weather Review*, *128*, 1697–1715.

Kim, B.-M., Lim, G.-H., & Kim, K.-Y. (2006). A new look at the midlatitude–MJO teleconnection in the Northern Hemisphere winter. *Quarterly Journal of the Royal Meteorological Society*, *132*, 485–503.

Kim, H., Kim, D., Vitart, F., Toma, V. E., Kug, J., & Webster, P. J. (2016). MJO propagation across the Maritime Continent in the ECMWF ensemble prediction system. *Journal of Climate*, *29*, 3973–3988.

Masato, G., Hoskins, B., & Woollings, T. J. (2012). Wave-breaking characteristics of midlatitude blocking. *Quarterly Journal of the Royal Meteorological Society*, *138*, 1285–1296.

Moon, J.-Y., Wang, B., & Ha, K.-J. (2011). ENSO regulation of MJO teleconnection. *Climate Dynamics*, *37*, 1133–1149.

Mundhenk, B. D., Barnes, E. A., & Maloney, E. D. (2016). Modulation of atmospheric rivers near Alaska and the US west coast by northeast Pacific height anomalies. *Journal of Geophysical Research: Atmospheres*, *121*, 12,751–12,765. https://doi.org/10.1002/2016JD025350

Peatman, S. C., Matthews, A. J., & Stevens, D. P. (2015). Propagation of the Madden–Julian oscillation and scale interaction with the diurnal cycle in a high-resolution GCM. *Climate Dynamics*, *45*, 2901–2918.

Rienecker, M. M., Suarez, M. J., Gelaro, R., Todling, R., Liu, J. BacmeisterE., Bosilovich, M. G., … Woollen, J. (2011). MERRA: NASA's Modern-Era Retrospective Analysis for research and applications. *Journal of Climate*, *24*, 3624–3648.

Seo, K.-H., & Lee, H.-J. (2017). Mechanisms for a PNA-like teleconnection pattern in response to the MJO. *Journal of Atmospheric Sciences*, *74*, 1767–1781.

Son, S., Lim, Y., Yoo, C., Hendon, H. H., & Kim, J. (2017). Stratospheric control of the Madden–Julian oscillation. *Journal of Climate*, *30*, 1909–1922.

Vitart, F. (2014). Evolution of ECMWF sub-seasonal forecast skill scores. *Quarterly Journal of the Royal Meteorological Society*, *140*, 1889–1899.

Vitart, F., & Molteni, F. (2010). Simulation of the Madden–Julian oscillation and its teleconnections in the ECMWF forecast system. *Quarterly Journal of the Royal Meteorological Society*, *136*, 842–855.

Vitart, F., Ardilouze, C., Bonet, A., Brookshaw, A., Chen, M., Codorean, C., … Zhang, L. (2017). The subseasonal to seasonal (S2S) prediction project database. *Bulletin of the American Meteorological Society*, *98*(1), 163–173.

Wallace, J. M., & Gutzler, D. S. (1981). Teleconnections in the geopotential height field during the Northern Hemisphere winter. *Monthly Weather Review*, *109*, 784–812.

Wilks, D. S. (2011). *Statistical methods in the atmospheric sciences* (676 pp.). London: Elsevier.